The Astrophysical Journal, 932:21 (9pp), 2022 June 10 https://doi.org/10.3847/1538-4357/ac660b

Radio Emission from Binary Ultracool Dwarf Systems

Melodie M. Kao[1,2,3,4] and J. Sebastian Pineda[5]
[1] University of California Santa Cruz, Department of Astronomy and Astrophysics, 1156 High Street, Santa Cruz, CA 95064, USA; melodie.kao@ucsc.edu
[2] Arizona State University, School of Earth and Space Exploration, 781 Terrace Mall, Tempe, AZ 85287, USA
[3] Heising-Simons Foundation 51 Pegasi b Fellow
[4] NASA Hubble Postdoctoral Fellow
[5] University of Colorado Boulder, Laboratory for Atmospheric and Space Physics, 3665 Discovery Drive, Boulder CO, 80303, USA
Received 2020 August 28; revised 2022 March 28; accepted 2022 April 8; published 2022 June 10

Abstract

Well-characterized binary systems will provide valuable opportunities to study the conditions that are necessary for the onset of both auroral and nonauroral magnetospheric radio emission in the ultracool dwarf regime. We present new detections of nonauroral "quiescent" radio emission at 4–8 GHz of the three ultracool dwarf binary systems GJ 564 BC, LP 415-20, and 2MASS J21402931+1625183. We also tentatively detect a highly circularly polarized pulse at 4–6 GHz that may indicate aurorae from GJ 564 BC. Finally, we show that the brightest binary ultracool dwarf systems may be more luminous than predictions from single-object systems.

Unified Astronomy Thesaurus concepts: Brown dwarfs (185); Binary stars (154); Magnetic fields (994); Radio continuum emission (1340)

1. Introduction

Since the first discovery of radio emission (Berger et al. 2001) from ultracool dwarfs with M7 and later spectral types, GHz radio observations of such objects have revolutionized our understanding of how magnetic activity evolves over the star-planet transition regime. Surveys of X-ray emission in the lowest-mass stars showed a sharp drop-off in coronal emissions at a spectral type M9.5 (Williams et al. 2014), with chromospheric Hα emission declining continuously across the L-dwarf regime (Schmidt et al. 2015; Pineda et al. 2016). Despite these declining diagnostics of magnetic activity, radio observations demonstrated persistently strong GHz emissions across the entire ultracool dwarf regime, revealing the emergence of radio aurorae (Hallinan et al. 2015; Kao et al. 2016; Pineda et al. 2017).

The radio component of ultracool dwarf aurorae manifests as periodically flaring and highly circularly polarized coherent electron cyclotron maser emission (Hallinan et al. 2007, 2008). This emission traces the fundamental cyclotron frequency of the local magnetosphere (Treumann 2006). Detections of GHz radio aurorae confirm that ultracool dwarfs at least as late as T6.5 can host strong kiloGauss magnetic fields (Route & Wolszczan 2012, 2016a; Williams & Berger 2015; Kao et al. 2016, 2018; Richey-Yowell et al. 2020).

Ultracool dwarfs also exhibit nonthermal and incoherent radio emission that is quasi-steady and weakly circularly polarized (e.g., Williams et al. 2015a; Kao et al. 2016, 2018). This "quiescent" radio emission is attributed to optically thin gyrosynchrotron emission (e.g., Berger et al. 2005; Osten et al. 2006; Williams et al. 2015b; Lynch et al. 2016) and can persist for years (e.g., Berger et al. 2008a; Kao et al. 2016, 2018). Furthermore, quiescent radio luminosities correlate with Hα luminosities in aurorae-emitting ultracool dwarfs, suggesting that the physical conditions underpinning ultracool dwarf radio aurorae may also be related to their quiescent radio emission (Pineda et al. 2017). Kao et al. (2019) argue that one plausible explanation is radiation belts analogous to the extended circumplanetary regions of high-energy electrons trapped in the magnetospheres of solar system planets (Sault et al. 1997; Bolton et al. 2004; Clarke et al. 2004; Horne et al. 2008). While the source of this magnetospheric plasma is unknown, flares are one possibility (e.g., Gizis et al. 2013; Paudel et al. 2018; Jackman et al. 2019; Paudel et al. 2020) and Kao et al. (2018, 2019) speculate that volcanic activity from planets could be another.

In this work, we examine radio emission in three ultracool dwarf binary systems. Such systems will provide valuable tests of ultracool dwarf magnetic activity. Unlike the field population, binaries can have precise observational constraints on individual masses and therefore ages (e.g., Konopacky et al. 2010; Dupuy & Liu 2017; Dupuy et al. 2019). Precisely known properties enable robust comparisons between individual objects and the conditions which power their radio emission. For instance, in two radio ultracool dwarf binary systems, only one component exhibits detectable GHz radio emission (Konopacky et al. 2012; Harding et al. 2013; Williams et al. 2015a; Forbrich et al. 2016). Why is one component radio bright but the other is not? Additional observations of well-characterized systems, such as those presented in this work, will help elucidate this question.

2. Targets

We present new observations of three binary systems using the *NSF*'s Karl G. Jansky Very Large Array (VLA; Perley et al. 2011) from program VLA 18B-283 (PI—Pineda). We selected these binary systems for their fast rotation. Pineda et al. (2017) showed that the fraction of ultracool dwarfs detected at radio frequencies rises as a function of projected rotational velocity $v \sin i$ for speeds $\gtrsim$35 km s^{-1}, which corresponds to a $\sim$3.5 hr period when viewed at an inclination of 90°. This strong dependence on rotation is consistent with existing theories for driving the electrodynamic engines of aurorae (e.g., Nichols et al. 2012; Turnpenney et al. 2017) and may be a requirement

Table 1
Targets

Object	SpT[c]	$v \sin i$[c] (km s^{-1})	a (au)	π (mas)	d (pc)	$\mu_\alpha \cos\delta$ (mas yr^{-1})	μ_δ (mas yr^{-1})	Ref
GJ 564 BC[a]	L4.0 ± 1.0 ; L4.0 ± 1.0	62 ± 4; 86 ± 6	$2.226^{+0.014}_{-0.013}$	54.9068 ± 0.0684	18.2127 ± 0.0227	−144.7 ± 0.8	−32.4 ± 0.7	1 4 3 2
J2140+16[b]	M8.0 ± 0.5 ; L0.5 ± 1.0	13 ± 2; 37 ± 3	4.71 ± 0.14	30.1972 ± 0.434	33.1 ± 0.5	−77.9 ± 0.776	−85.637 ± 0.707	1 4 3
LP 415−20	M6.0 ± 1.0 ; M8.0 ± 0.5	40 ± 5; 37 ± 4	3.73 ± 0.12	25.1963 ± 0.5117	39.6884 ± 0.8060	−134.716 ± 0.912	−38.416 ± 0.619	1 4 3

Notes.
[a] Also known as HD 130948B.
[b] 2MASS J21402931+1625183.
[c] Listed values are for the primary and secondary, respectively.
References— (1) (Dupuy & Liu 2017); (2) (Faherty et al. 2009); (3) (Gaia Collaboration 2018); (4) (Konopacky et al. 2012).

for generating the strong dipolar magnetic field topologies (Shulyak et al. 2017) that are a critical ingredient to powering ultracool dwarf auroral processes (Pineda et al. 2017).

Table 1 summarizes the properties of our targets and we discuss them in further detail below.

GJ 564 BC is also known as HD 130948BC, a benchmark brown dwarf system orbiting a solar analog (Dupuy et al. 2009). It was discovered through adaptive optics imaging (Potter et al. 2002) and is the nearest binary in our observation sample. This 0.44 ± 0.04 Gyr system consists of two nearly equal-mass L4 dwarfs on a ∼10 yr orbit with masses of $59.8^{+2.0}_{-2.1}$ and $55.6^{+2.0}_{-1.9}$ M_J for the B and C components, respectively (Dupuy & Liu 2017). This system is unresolved from GJ 564 A except in adaptive optics imaging. Hα emission for this system is unknown because the binary is unresolved in spectroscopic observations from the solar type primary.

2MASS J21402931+1625183 was first identified as a binary system by Close et al. (2002, 2003). Earlier attempts to determine masses for this system suggested a large primary to secondary mass ratio (∼4; Konopacky et al. 2010). Most recently, Dupuy & Liu (2017) reported that the primary has a mass of 114^{+10}_{-12} M_J and the secondary has a mass of 69^{+8}_{-9} M_J. These updated values confirm the suggestion by Konopacky et al. (2010) that their estimated mass ratio was likely too high. Dupuy & Liu (2017) did not provide an age estimate for this system, but Martin et al. (2017) reported that gravity-sensitive indices in the near-IR spectrum of this system indicate that it is not young (FLD-G classification, $\gtrsim$200 Myr). Gizis et al. (2000) report an Hα EW of 0 Å. This low-eccentricity system ($e = 0.196 \pm 0.007$) has a ∼24.4 yr orbit.

LP 415-20 was first identified as a binary by Siegler et al. (2003). It is another unequal-mass binary system with masses of 156^{+17}_{-18} M_J and 92^{+16}_{-18} M_J for the primary and secondary, respectively (Dupuy & Liu 2017). However, Dupuy & Liu (2017) note that the mass of the primary component is much higher than expected for its luminosity and speculate that the primary may be an unresolved unequal-mass binary. If so, the primary would likely be comprised of clearly ultracool dwarf ∼100 M_J and ∼50 M_J components, whose combined light is estimated as an M6 object, although spectral decomposition suggests spectra are consistent with templates of types M5-M7. This high eccentricity ($e = 0.706^{+0.011}_{-0.012}$) system has a ∼14.8 yr orbit. The model-derived age of the secondary component is $5.0^{+1.9}_{-4.7}$ Gyr, and an unresolved binary system for the primary component points to a model-derived age of at least several hundred Myr. Using BANYAN Σ (Gagné et al. 2018), we find that LP 415-20 is a likely member of the Hyades Cluster with $\geqslant$99% probability (750 ± 100; Brandt & Huang 2015) when using the Gaia parallax and proper motion data along with a mean system radial velocity of 40.8 ± 1.4 km s^{-1} (Konopacky et al. 2010). Miles-Páez et al. (2017) report significant photometric variability in the combined light of the system with a periodicity of ∼4.36 hr. The system also shows Hα in emission, with an EW measurement of 4.4 Å (Gizis et al. 2000).

3. Observations and Calibrations

We summarize the target observations in Table 2. For GJ 564 BC, we obtained two 2 hr observing blocks with the VLA for four total hours on sky. For 2MASS J21402931 +1625183 and LP 415-20, we obtained one 5 hr observing block each.

We calibrated our measurement sets using nearby phase calibrators and the standard VLA flux calibrators 3C147 and 3C286. Typical full-bandwidth sensitivities at C configuration for 2 and 5 hr integration blocks with 3.5 GHz bandwidth (to account for RFI excision) centered at 6.0 GHz are 2.1 μJy and 1.4 μJy, respectively, and reach absolute flux calibration accuracy of ∼5%.

To account for phase errors that can systematically reduce flux densities, the National Radio Astronomy Observatory (NRAO) recommended phase calibration cycle times of ∼25 minutes for observations at 4–8 GHz in C configuration when these observations took place. We adhered to these guidelines for our observations. For GJ 564 BC, we alternated between a nearby phase calibrator and the target with integration times of 2 and 23.75 minutes, respectively, for a total cycle time of 25.75 minutes. For 2MASS J21402931+1625183, these integration times were 2 and 20.6 minutes, for a total cycle time of 22.6 minutes. For LP 415-20, the integration times were 2 and 23.5 minutes, for a total cycle time of 25.5 minutes.

Sidelobes from a bright ∼31.3 mJy object located ∼3.3 arcmin to the northeast lead to poor initial image quality for 2MASS J21402931+1625183. We self-calibrate its target field using this bright object to improve our image rms noise by a factor of 12, from 43.4 μJy to 3.6 μJy.

We did not observe polarization calibrators, but the absence of polarization calibration is not a limiting factor for our analysis. Polarization leakage at typical levels of 2%–3% results in spurious Stokes V (circularly polarized) flux densities of ∼1.2 μJy for our brightest source, which is less than the noise floor.

Table 2
Summary of Observations

Object	Obs. Date	Time on Source (hh:mm:ss)	Synthesized Beam ($'' \times ''$)	Phase Calib.	Flux Calib.
GJ 564 BC	2019 Jan 21	01:34:10	4.17×3.59	J1443+2501	3C286
	2019 Feb 05	01:33:59	3.15×2.55	J1443+2501	3C286
J2140+16	2019 Feb 03	04:15:16	4.10×3.65	J2139+1423	3C286
LP 415−20	2018 Dec 28	04:15:30	4.09×3.71	J0431+2037	3C147

Note. All observations were at 4–8 GHz and taken during C configuration at the VLA.

Table 3
Flux Density Measurements

	Stokes I			Stokes V				
Object	Peak Brightness uvmodelfit (μJy beam^{-1})	Peak Brightness imfit (μJy beam^{-1})	Integrated F_ν imfit (μJy)	$[L_\nu]$[a] log[(erg s^{-1} Hz^{-1})]	F_ν (μJy)	$[L_\nu]$[a] log[(erg s^{-1} Hz^{-1})]	% Circ. Poln.[a]	Notes
GJ 564 BC	22.7 ± 2.7	19.4 ± 4.5	21.6 ± 8.7	12.9	<12.0	<12.7	$\leqslant 58.8^{+24.0}_{-19.6}$	Epoch: 2019 Jan 21
	31.3 ± 2.2	30.1 ± 3.7	38.7 ± 7.6	13.1	<9.3	<12.6	$\leqslant 30.4^{+12.7}_{-9.8}$	Epoch: 2019 Feb 05
J2140+1625	15.6 ± 1.7	20.1 ± 3.3	16.0 ± 5.0	13.4	<9.0	<13.4	$\leqslant 43.6^{+20.8}_{-13.8}$	
LP 415−20	24.1 ± 1.4	22.9 ± 2.5	24.9 ± 4.6	13.6	<6.5	<13.1	$\leqslant 28.0^{+11.2}_{-9.1}$	

Notes. We measured Stokes I flux densities in two ways: (1) fitting the cleaned image with the CASA task `imfit` and (2) fitting the UV visibilities with the task `uvmodelfit` after subtracting other sources in the primary beam. `imfit` returns both peak brightness and integrated flux density. For point sources, the peak flux density should be consistent with the integrated flux density. `uvmodelfit` returns formal errors that are underestimated by at least a factor $\sqrt{\chi^2_R}$, which we have corrected for in the reported errors. No Stokes V sources were detected, so we report the $3\sigma_{\rm rms}$ upper limit.
[a] Calculated using the peak F_ν fitted with `imfit`. Uncertainties in log-luminosity are <0.1 and do not affect the presented analysis.

We initially processed each measurement set with the VLA CASA 5.6.2 Calibration Pipeline, after which we flagged all remaining radio frequency interference (RFI) and checked all calibrations. As a rule, all data between 4.0–4.4 GHz was discarded due to extremely bright and persistent RFI. We obtained absolute flux by bootstrapping flux densities with the observed flux calibrators.

4. Imaging

We produced Stokes I and Stokes V (total and circularly polarized intensities, respectively) images for the entire observing block of each object with the CASA `tclean` routine. For GJ 564 BC and LP 415-20, we model the frequency dependence of sources with three terms to account for curvature in the spectrum. We also use natural weighting for best point-source sensitivity, multiscale cleaning with a bias of 0.5 to more heavily weighted point sources, and set the cell size to $0\farcs3 \times 0\farcs3$.

For 2MASS J21402931+1625183, dynamic range limits its imaging. To suppress sidelobes from bright sources in the field of view, we use Briggs weighting and set `robust=0.5`. Bright sources outside of the primary beam cause image artifacts due to noncoplanar baselines. We mitigate these artifacts with *w*-projection and reduce some computational overhead by slightly increasing the cell size to $0\farcs4 \times 0\farcs4$. Finally, we model the frequency dependence of sources with four terms to account for artifacts that cannot be satisfactorily modeled with three terms.

We searched for a point source at the proper motion-corrected coordinates of each target by eye and detect radio emission from all three of our targets, including for both epochs of GJ 564 BC.

For each object, we fit the flux density of the source using two methods. Prior to flux fitting, we added phase delays to our visibility data to transform the phase center of our data to the measured locations of our targets using the CASA task `fixvis`. Shifting to the phase center allows for flux density measurements with the CASA task `uvmodelfit`, which requires that the target be at or very near the phase center.

After cleaning the target field, we subtracted models for all sources except for the target using the CASA task `uvsub`. Then, we fit the calibrated visibilities with a point-source model using the CASA task `uvmodelfit`. We also fit an elliptical Gaussian point source to the cleaned image of each object using the CASA task `imfit`. Table 3 gives measured flux densities and percent circular polarizations for detected objects and 3σ upper limits on the flux densities for undetected objects. Figure 1 shows Stokes I and V images for all targets.

5. Time Series

We also generated time series for each object's right- and left-circularly polarized (rr- and ll-correlations) emission. To do this, we time-averaged and frequency-averaged the

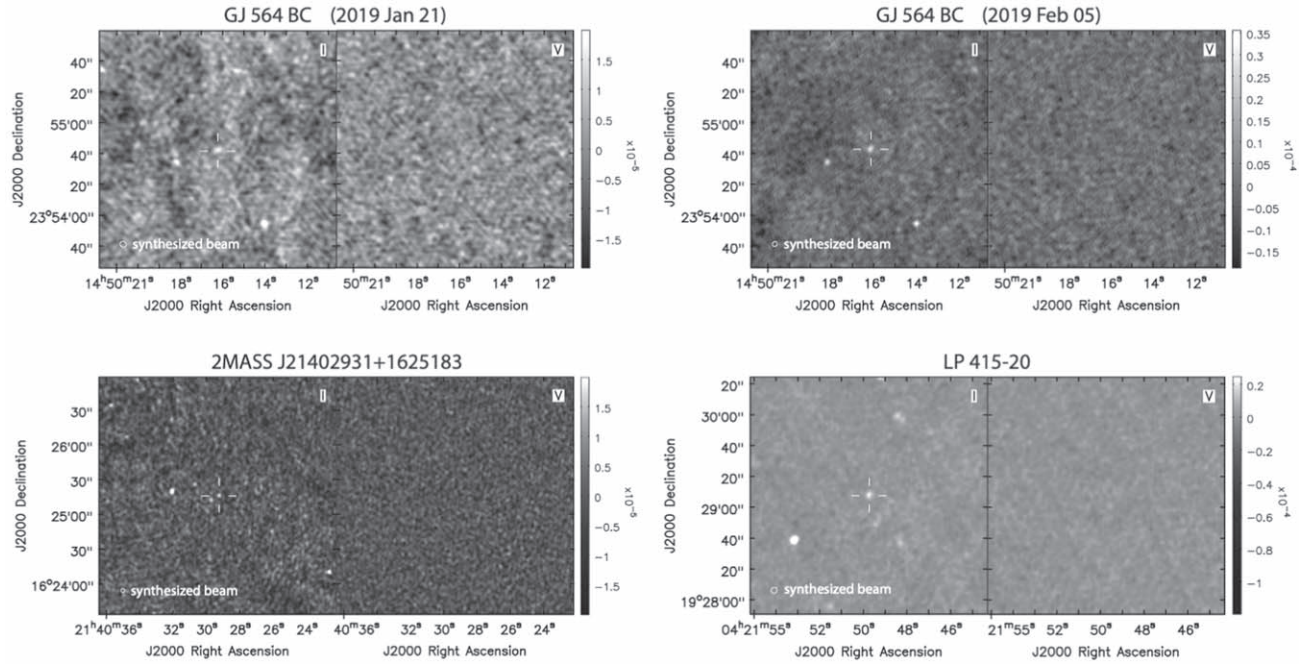

Figure 1. 4–8 GHz Stokes I and V images averaged over the full observing block for each target. Crosshairs indicate detected flux at the expected locations of our targets. No Stokes V emission was detected from our targets.

phase-centered data into 10 s, 30 s, and 60 s time resolutions each for 4–8 GHz, 4–6 GHz, and 6–8 GHz sub-bands using the averaging functions available with CASA's plotting tool `plotms`, and we exported the averaged time series of the real component of the phase-centered visibilities. Using these different time resolutions, we check for possible substructures in identified candidate pulses (see below) and also check that such candidate pulses are present for all time resolutions.

We then searched these time series for candidates of highly circularly polarized pulses indicative of auroral emission using the following revision of the procedure described in Kao et al. (2018):

1. Calculate a time series t_q for slowly varying quiescent emission by smoothing the raw time series with a Gaussian kernel that has a width of 10% of the total time on source.
2. Construct a time series t_p for pulse searching by smoothing the raw time series with a Gaussian kernel that has a width of 1% of the total time on source. This mitigates residual noise spikes that may not have been identified for excision by both the CASA data reduction pipeline and our own manual examination of the data, which are much narrower than observed radio aurorae pulses that have durations at least as long as several minutes (e.g., Berger et al. 2001; Burgasser & Putman 2005; Hallinan et al. 2007, 2008; Berger 2006; Berger et al. 2009; Route & Wolszczan 2012, 2016b; Williams et al. 2015a; Gizis et al. 2016; Kao et al. 2016, 2018; Zhang et al. 2020).
3. Subtract t_q from t_p to obtain a residual time series t_r without the quiescent component.
4. Identify peaks with at least $2\sigma_{\rm rms}$, where $\sigma_{\rm rms}$ is the rms of t_r. This lower significance accounts for the possibility that t_r may have pulses that could elevate $\sigma_{\rm rms}$ and prevent the identification of weaker pulses. Thus, we remove the strongest peaks in the first iteration of this procedure and then repeat it with an updated $\sigma_{\rm rms}$ that excludes any initially identified peaks.
5. Calculate the FWHM of identified peaks.
6. Remove the full width of each identified peak from t_r, where we define the full width of each peak as three times the FWHM. This gives the updated residual time series $t_{r,u}$.
7. Repeat steps 4–6, using $t_{r,u}$ for calculating $\sigma_{\rm rms}$ and t_r for peak searching. For this iteration, we also require a peak significance threshold of $3\sigma_{\rm rms}$. Returned peaks are candidate pulses. Note that by using t_r for the peak search, this procedure does not inherit identified peaks using the lower significance from the first iteration. Instead, all candidate pulses identified by the full procedure must meet a $3\sigma_{\rm rms}$ significance.

We emphasize that the sole function of the procedure outlined above is to aid in identifying candidate pulses in a repeatable manner. Final confirmation of identified candidate pulses relies on human judgment. Figure 2 shows the 4–8 GHz time series for each object.

We detect one candidate pulse from GJ 564 BC during its first epoch which is present for all time series resolutions. Comparing the 4–6 GHz and 6–8 GHz time series shows that the pulse appears only in the lower subband (Figure 3). To confirm this pulse, we image over the time interval of its FWHM at 4–6 GHz and measure its Stokes I (95 ± 27 μJy) and Stokes V (125 ± 24 μJy) flux densities. While Stokes V flux densities cannot physically exceed Stokes I flux densities, the measured Stokes I and V flux densities are consistent within $3\sigma_{\rm rms}$ and correspond to a lower bound percent circular polarization of $\geqslant$38% with 99.7% confidence. For comparison, imaging outside of the full width of the identified pulse using the full bandwidth yields a Stokes I quiescent emission flux density of 19.2 ± 4.9 μJy, and no Stokes V source is detected to a $3\sigma_{\rm rms}$ significance of $\leqslant$15.0 μJy.

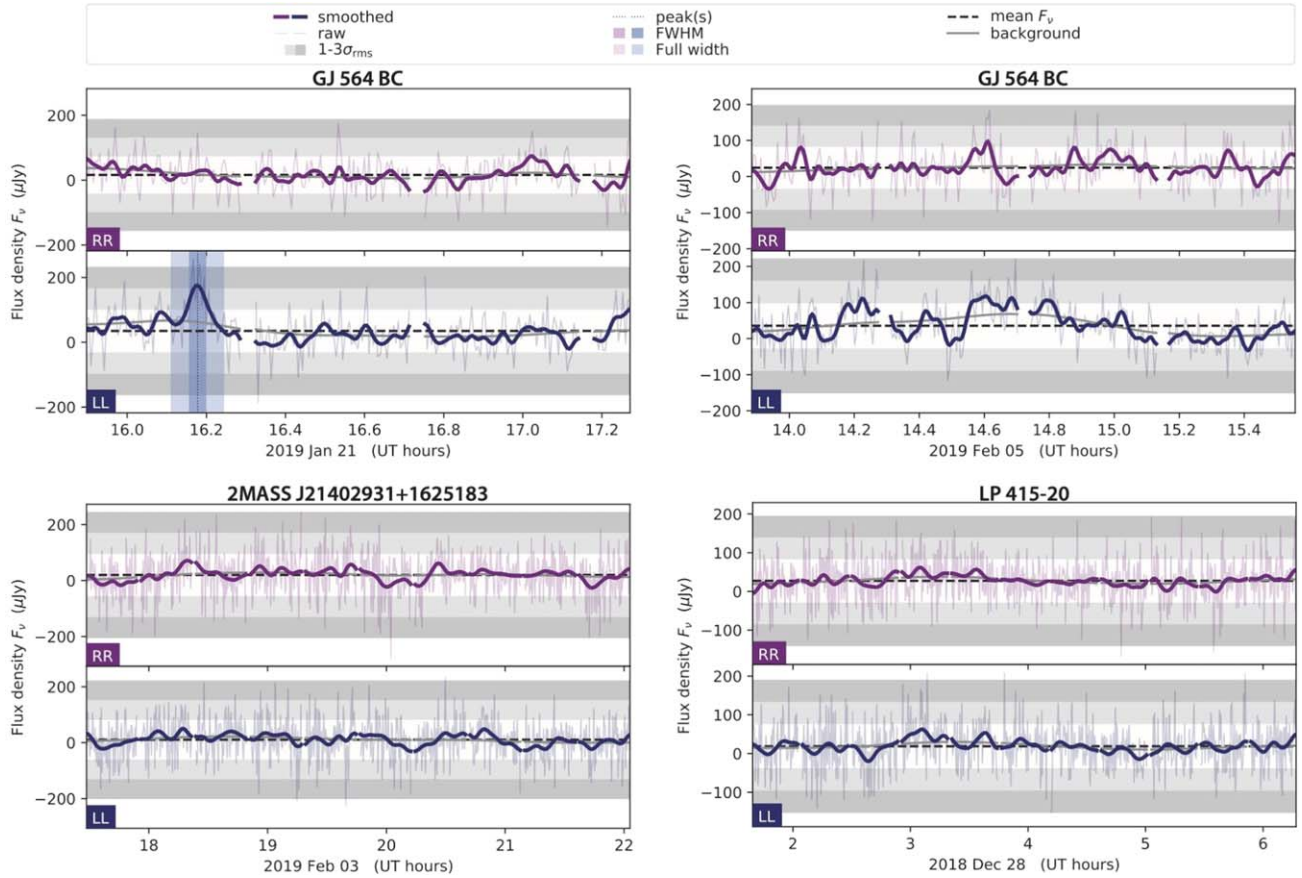

Figure 2. 4–8 GHz right- and left-circularly polarized (RR and LL, respectively) time series for detected objects with 10 s averaging. Gaps in time series correspond to phase calibration scans and rms values shown in gray correspond to the rms of the raw time-averaged data. A left-circularly polarized candidate pulse was detected in the 2019 January 21 epoch for GJ 564 BC, and shaded regions around that pulse show the calculated FWHM and full-width regions.

However, the target is difficult to distinguish from noise peaks in the image (Figure 4), so we bootstrap the significance of the measured Stokes I and Stokes V flux densities by fitting a point source in 10,000 randomly drawn fitting regions of size 50×50 pixels. We find that the Stokes I flux density has a significance of 98.5% and the Stokes V flux density has a significance of 99.9%. We therefore classify this candidate pulse as only a tentative detection. Similarly, the Stokes I flux density of the quiescent emission is also tentative, corresponding to a 99.8% significance.

We did not identify any candidate pulses from 2MASS J21402931+1625183 and LP 415-20 despite covering their likely full rotation periods. However, we note that our chosen time-averaging is only sensitive to pulses that are at least as bright as a peak flux of ∼100–200 μJy, or ∼5–10× brighter than their measured quiescent emission. Fainter pulses may exist to which our observations are not sensitive.

6. Discussion

We have detected radio emission from each of our three targets. In comparison, volume-limited radio surveys yield detection rates between ∼5% and 10% for M, L, and T ultracool dwarfs (Antonova et al. 2013; Lynch et al. 2016; Route & Wolszczan 2016b). The high success rate of our small sample suggests that binary ultracool dwarf systems with at least one rapidly rotating component ($v \sin i \gtrsim 35\ \mathrm{km\ s^{-1}}$) may be promising candidates for radio studies.

Our high detection rate is subject to small number statistics, and detection rates in general do not account for systematics like observational sensitivity or objects' intrinsic magnetospheric luminosity. In a forthcoming paper, we modify the occurrence rate framework developed by M. M. Kao & E. Shkolnik (2022, in preparation) for single-object systems to allow for direct comparisons of radio occurrence rates between binary and single-object systems.

Another possible contributing factor to our high detection rate is that binaries may be intrinsically brighter at radio frequencies than single-object systems. This is because binaries have twice as many components that can produce magnetospheric radio emission as single-object systems do. Indeed, we compiled all available measurements of detected quiescent radio emission from binary ultracool dwarfs in the literature in Table 4 and show in Figure 5 that their mean quiescent radio luminosities are brighter than detected single objects.

Intriguingly, the brightest binary systems may exceed the luminosities predicted from single objects. We expect that binary luminosities will not exceed two times the maximum luminosity of single objects if binarity does not affect the luminosities of individual binary components. In Figure 5, we show that the brightest detected single systems cannot account for the high luminosities of the brightest detected binaries. This figure accounts for an individual object's intrinsic variability by including measurements from repeated observations of detected objects.

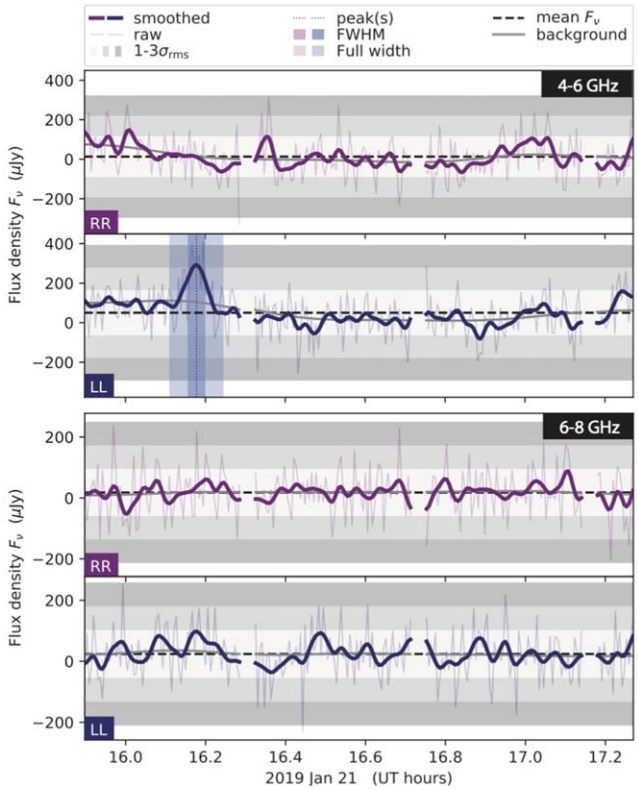

Figure 3. 4–6 GHz and 6–8 GHz right- and left-circularly polarized (RR and LL, respectively) time series for GJ 564 BC. Shaded regions around that pulse show the calculated FWHM and full-width regions. The candidate pulse appears to drop out at 6–8 GHz.

One immediate implication is that binary systems at farther distances than single objects may be detectable, increasing the number of observationally accessible systems. For instance, our targets 2MASS J21402931+1625183 and LP 415-20 are the most distant radio-bright ultracool dwarfs that have been detected at GHz frequencies to date, with distances of 33.1 ± 0.5 and 39.6884 ± 0.8060 pc, respectively. Before this work, the most distant radio-bright ultracool dwarf system was the binary 2MASS J09522188-1924319 (29.0 ± 0.13 pc) (McLean et al. 2012; Gaia Collaboration 2018). For comparison, the most distant detected single object is the L8.5 dwarf 2MASS J10430758+2225236 (Kao et al. 2016, 2018) at 16.4 ± 0.2 pc (Schmidt et al. 2010).

In Figure 6, we also compare the quiescent radio luminosities of our targets to their Hα luminosities, which Pineda et al. (2017) showed correlation in aurorae-emitting ultracool dwarfs. We convert Hα equivalent widths to $L_{\mathrm{H}\alpha}/L_{\mathrm{bol}}$ using the χ values from Schmidt et al. (2014). For systems without measured L_{bol} by Dupuy & Liu (2017), we use the Filippazzo et al. (2015) relations between spectral type and L_{bol}.

For LP 415-20, we do not detect any circularly polarized radio pulses that could indicate the presence of aurorae. While its Hα and quiescent radio luminosities cannot conclusively rule in or rule out the possibility that this system may exhibit radio aurorae in follow-up observations, we note that its strong Hα emission is slightly rightward of the proposed auroral correlation and is similar to other late M dwarf systems that do not show periodic radio pulses.

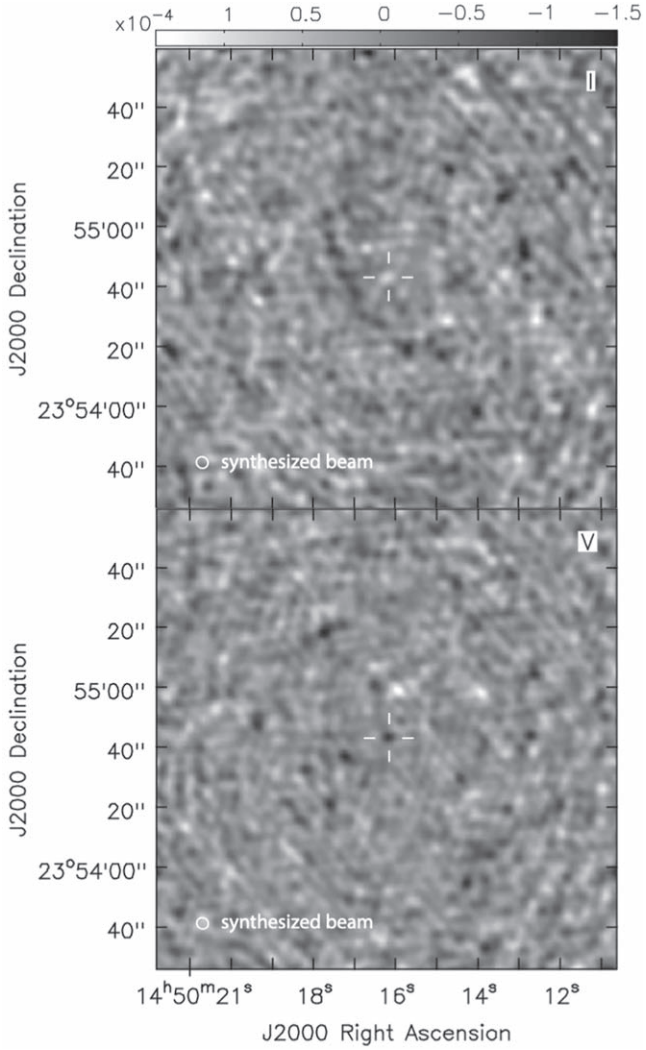

Figure 4. Image of GJ 564 BC over the FWHM of its identified candidate pulse. The target is visually indistinguishable from noise peaks in Stokes I and marginally distinguishable in Stokes V. Bootstrapping yields a significance of 98.5% for the Stokes I flux density and 99.9% for the Stokes V flux density. We classify this pulse as tentative rather than confirmed.

For 2MASS J21402931+1625183, we do not observe radio pulses in our data. If this system later proves to be auroral, its quiescent radio luminosity predicts an Hα luminosity of $[L_{\mathrm{H}\alpha}] \approx 24.8$ [erg s^{-1}] though scatter likely exists along the proposed auroral radio-Hα correlation. This translates to an EW of 0.7 Å if the emission originates from the M8 dwarf or an EW of 3 Å for the L0.5 dwarf. Gizis et al. (2000) reported an Hα EW of 0 Å, but they note that their Hα measurements should be taken with caution due to observing challenges. In particular, their data suggests that they may have had difficulty detecting Hα emission at the 0.7 Å level. In particular, they measure a nonzero EW < 1 Å for only one target in their sample of 60 late M and early L dwarfs, yet most objects in this spectral type range exhibit Hα emission. Additionally, because their observations do not resolve individual binary components, Hα emission on the faster rotating L dwarf may be obscured by the continuum of the brighter M8 dwarf. If this is the case and it exhibited weak radio pulses below our detection threshold, then resolved spectroscopy of the binary may yield a confident Hα detection.

Table 4
Specific Luminosities for Detected Quiescent Radio Emission in Binary Ultracool Dwarf Systems

Object Name	Other Name	SpT	π (mas)	d (pc)	Ref	F_ν (μJy)	$[L_\nu]$[a] log[(erg s^{-1} Hz^{-1})]	Ref
2MASS J00043484 −4044058	GJ 1001 B	L5+L5	82.0946 ± 0.3768	12.1811 ± 0.0559	30	100.0 ± 8.3	13.2	20
2MASS J00275592 +2219328	LP349−25	M7+M8	69.2 ± 0.9	14.5 ± 0.2	13	262 ± 40	13.8	23
						320 ± 21	13.9	23
						338 ± 54	13.9	23
						365 ± 16	14.0	24
						383 ± 27	14.0	23
2MASS J04234858 −0414035	SDSS J042348.57 −041403.5	L6.5+T2	67.8584 ± 1.5052	14.7366 ± 0.3269	30	15.4 ± 1.2	12.6	19
						26.7 ± 3.1	12.8	18
WISE J072003.20 −084651.2AB		M9+T5	142 ± 38	7 ± 2	26	15 ± 3	11.9	10
2MASS J12560183 −1257276a	VHS J125601.92 −125723.9a	M7.5 +M7.5	78.8 ± 6.4	12.7 ± 1.0	15	60 ± 3	13.1	16
2MASS J13153094 −2649513AB		L3.5+T7	53.8729 ± 1.1265	18.5622 ± 0.3881	30	370 ± 50	14.2	9
2MASS J13142039 +1320011	NLTT 33370	M7.0 +M7.0	57.9750 ± 0.0450	17.2488 ± 0.0134	12	1099 ± 18	14.6	21
						1032 ± 16	14.6	21
GJ 564 BC	HD 130948B	L4+L4	54.9068 ± 0.0684	18.2127 ± 0.0227	30	19.4 ± 4.5	12.9	1
						30.1 ± 3.7	13.1	1
2MASS J21402931 +1625183		M8+L0.5	30.1972 ± 0.4340	33.1157 ± 0.4759	30	20.1 ± 3.3	13.4	1

Notes. This table does not include the M7+M7 binary 2MASS J09522188-1924319 due to the possibility that the radio emission detected from this object may be flaring rather than quiescent emission. McLean et al. (2012) detected 233 ± 15 *mu*Jy emission from this object, which corresponds to $[L_\nu] = 14.4$. However, they reported that follow-up observations at 4.96 and 8.46 GHz after the initial detection did not yield a detection to a limit of 69 μJy, or a factor of 2.4 below the original detection. They concluded that the initial detection was likely a flare or that 2MASS J09522188-1924319 exhibits long-term variability. We also exclude LP 415-20 because of compelling evidence that the primary component of this system may in fact be unresolved ultracool dwarf binaries (Dupuy & Liu 2017).

[a] Uncertainties in log-luminosity are <0.1 and do not affect the presented analysis.

[b] McLean et al. (2012); Forbrich et al. (2016), and Williams et al. (2015a) also observe 2MASS J13142039+1320011 at radio frequencies but do not separately report quiescent emission.

References—(1) This paper; (2) Berger et al. (2001); (3) Berger (2002); (4) Berger et al. (2005); (5) Berger (2006); (6) Berger et al. (2008b); (7) Berger et al. (2008a); (8) Berger et al. (2009); (9) Burgasser et al. (2013); (10) Burgasser et al. (2015); (11) Burgasser & Putman (2005); (12) Dupuy et al. (2016); (13) Dupuy & Liu (2017); (14) Faherty et al. (2012); (15) Gauza et al. (2015); (16) Guirado et al. (2018); (17) Hallinan et al. (2006); (18) Kao et al. (2016); (19) Kao et al. (2018); (20) Lynch et al. (2016); (21) McLean et al. (2011); (22) Osten et al. (2006); (23) Osten et al. (2009); (24) Phan-Bao et al. (2007); (25) Richey-Yowell et al. (2020); (26) Scholz (2014); (27) Schmidt et al. (2010); (28) Williams et al. (2013); (29) Williams & Berger (2015); (30) Gaia Collaboration (2018).

Finally, GJ 564 BC does not have an available Hα measurement in the literature though we detect a tentative radio burst that may indicate aurorae. If its tentative radio burst is indeed auroral in nature, its averaged quiescent radio flux predicts an Hα luminosity of $[L_{\rm H\alpha}] \approx 24.0$ [erg s^{-1}], which translates to an EW of 2.6 Å.

The radio observations presented here and the growing population of known radio-bright ultracool dwarf binaries will also be valuable benchmarks for calibrating magnetic models in the substellar mass regime. For instance, Mullan & MacDonald (2010) found that nonmagnetic models cannot replicate both the observed luminosity and $T_{\rm eff}$ of GJ 564 BC. The addition of a strong internal magnetic field corresponding to a $\gtrsim$400 G surface field strength impedes the onset of convection and helps resolve this issue. If follow-up observations confirm that the tentative pulse that we observe from GJ 564 BC is indeed auroral in nature, its surface-averaged magnetic field may be at least as strong as $\geqslant$1.3 kG (Kao et al. 2016).

Additional detections and confirmations of the circularly polarized auroral pulses that usually coexist with ultracool dwarf quiescent radio emission (e.g., Berger et al. 2001; Hallinan et al. 2007, 2008; Williams & Berger 2015; Kao et al. 2016, 2018) will yield more direct tests to calibrate such magnetism-dependent models.

7. Conclusions

Binary ultracool dwarf systems are promising targets for radio studies of their magnetic activity due to the relative ease of constraining the masses and ages of their individual components compared to single objects. Here, we show that they may also be promising targets because the quiescent radio emission of the brightest binaries may be overly luminous compared to naively pairing single-object systems.

We present new radio observations and detections of quiescent radio emission from three binary systems that were previously not known to be radio emitters. Our detections of 2MASS J21402931+1625183 and LP 415-20 represent the farthest known radio-bright ultracool dwarfs sans coherent radio emission. We also tentatively detect possible 4–6 GHz aurorae from GJ 564 BC. If follow-up monitoring shows that our targets are auroral in nature, we predict their Hα luminosities based on the proposed radio-Hα correlation by

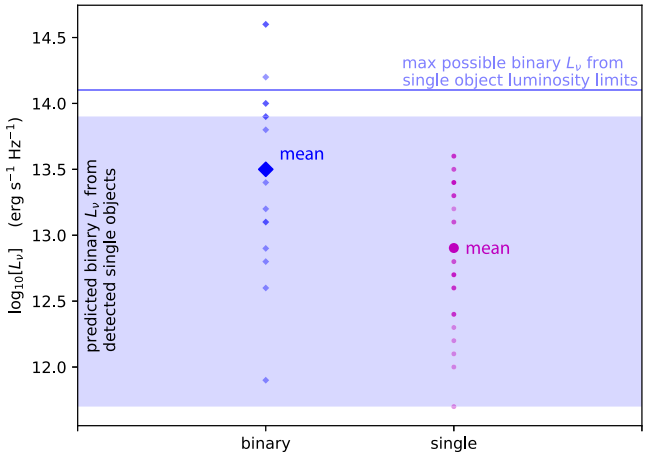

Figure 5. Radio luminosities of detected quiescent radio emission from ultracool dwarfs (translucent small markers) and mean values for binary vs. single objects (solid big markers). Uncertainties are less than marker sizes. The shaded region corresponds to predicted binary luminosity ranges if individual binary components follow the same luminosity distribution as single objects. Detected binary ultracool dwarf systems are on average more radio luminous than single objects. We use the compilations of single objects in M. M. Kao & E. Shkolnik (2022, in preparation), which includes 82 ultracool M dwarfs, 74 L dwarfs, and 23 T/Y dwarfs.

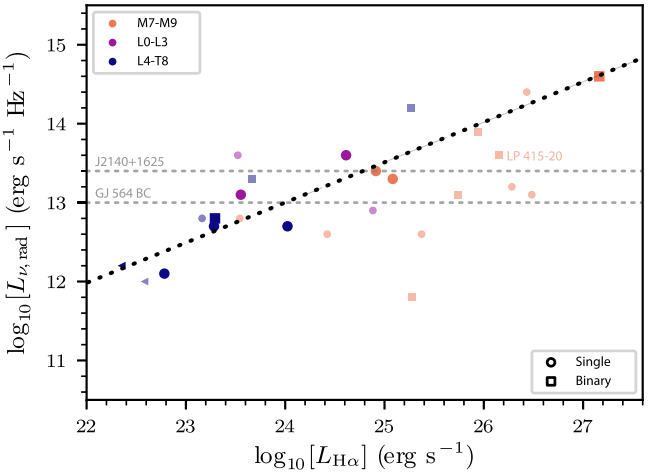

Figure 6. Radio vs. Hα luminosities for binary and single-object systems with detected quiescent radio emission for systems that are confirmed auroral emitters (solid) vs. those that are not (translucent), depicting the correlation between quiescent radio and Hα luminosities (black dotted line) by Pineda et al. (2017). Only one of our observed targets, LP 415-20, has a nonzero or existing Hα measurement. Gray dashed lines correspond to the measured radio luminosities for the other two targets. Uncertainties are comparable to or smaller than the symbol sizes, except for binaries that cannot be resolved. For these systems, we consider total emission as coming from a single object with bolometric luminosity consistent with a single object that has an average spectral type of pair, which will produce additional systematics at the ~0.3 dex level. These systematics are not relevant to our science discussion, so we do not show them here.

Pineda et al. (2017). The three new detections that we present increase the number of known radio ultracool dwarf systems to 25. Existing radio detections of ultracool dwarf systems suggest that rapidly rotating objects with $v \sin i \gtrsim 35\ \mathrm{km\ s^{-1}}$ may be promising targets for radio studies. Our observations support this picture.

MK especially thanks Jackie Villadsen for her help in troubleshooting target calibration and imaging. Support was provided by NASA through the NASA Hubble Fellowship grant HST-HF2-51411.001-A awarded by the Space Telescope Science Institute, which is operated by the Association of Universities for Research in Astronomy, Inc., for NASA, under contract NAS5-26555; and by the National Radio Astronomy Observatory. The National Radio Astronomy Observatory is a facility of the National Science Foundation (NSF) operated under a cooperative agreement by Associated Universities, Inc. This work is based on observations made with the NSF's Karl G. Jansky Very Large Array (VLA). This research has made use of the SIMBAD and VizieR databases, operated at CDS, Strasbourg, France; and the European Space Agency (ESA) mission Gaia (https://www.cosmos.esa.int/gaia), processed by the Gaia Data Processing and Analysis Consortium (DPAC, https://www.cosmos.esa.int/web/gaia/dpac/consortium).

Facility: JVLA.

Software: CASA (McMullin et al. 2007), Astropy (Price-Whelan et al. 2018), Matplotlib (Hunter 2007), Numpy (van der Walt et al. 2011), Scipy (Virtanen et al. 2020).

ORCID iDs

Melodie M. Kao https://orcid.org/0000-0001-5125-1414
J. Sebastian Pineda https://orcid.org/0000-0002-4489-0135

References

Antonova, A., Hallinan, G., Doyle, J. G., et al. 2013, A&A, 549, A131
Berger, E. 2002, ApJ, 572, 503
Berger, E. 2006, ApJ, 648, 629
Berger, E., Ball, S., Becker, K. M., et al. 2001, Natur, 410, 338
Berger, E., Basri, G., Gizis, J. E., et al. 2008a, ApJ, 676, 1307
Berger, E., Gizis, J. E., Giampapa, M. S., et al. 2008b, ApJ, 673, 1080
Berger, E., Rutledge, R. E., Phan-Bao, N., et al. 2009, ApJ, 695, 310
Berger, E., Rutledge, R. E., Reid, I. N., et al. 2005, ApJ, 627, 960
Bolton, S. J., Thorne, R. M., Bourdarie, S., de Pater, I., & Mauk, B. 2004, in Jupiter's Inner Radiation Belts, ed. F. Bagenal, T. E. Dowling, & W. B. McKinnon (Cambridge: Cambridge Univ. Press), 671
Brandt, T. D., & Huang, C. X. 2015, ApJ, 807, 58
Burgasser, A. J., Melis, C., Todd, J., et al. 2015, AJ, 150, 180
Burgasser, A. J., Melis, C., Zauderer, B. A., & Berger, E. 2013, ApJL, 762, L3
Burgasser, A. J., & Putman, M. E. 2005, ApJ, 626, 486
Clarke, J. T., Grodent, D., Cowley, S. W. H., et al. 2004, in Jupiter's Aurora, ed. F. Bagenal, T. E. Dowling, & W. B. McKinnon (Cambridge: Cambridge Univ. Press), 639
Close, L. M., Siegler, N., Freed, M., & Biller, B. 2003, ApJ, 587, 407
Close, L. M., Siegler, N., Potter, D., Brand ner, W., & Liebert, J. 2002, ApJL, 567, L53
Dupuy, T. J., Forbrich, J., Rizzuto, A., et al. 2016, ApJ, 827, 23
Dupuy, T. J., & Liu, M. C. 2017, ApJS, 231, 15
Dupuy, T. J., Liu, M. C., Best, W. M. J., et al. 2019, AJ, 158, 174
Dupuy, T. J., Liu, M. C., & Ireland, M. J. 2009, ApJ, 692, 729
Faherty, J. K., Burgasser, A. J., Cruz, K. L., et al. 2009, AJ, 137, 1
Faherty, J. K., Burgasser, A. J., Walter, F. M., et al. 2012, ApJ, 752, 56
Filippazzo, J. C., Rice, E. L., Faherty, J., et al. 2015, ApJ, 810, 158
Forbrich, J., Dupuy, T. J., Reid, M. J., et al. 2016, ApJ, 827, 22
Gagné, J., Mamajek, E. E., Malo, L., et al. 2018, ApJ, 856, 23
Gaia Collaboration, Brown, A. G. A., & Vallenari, A. 2018, A&A, 616, A1
Gauza, B., Béjar, V. J. S., Pérez-Garrido, A., et al. 2015, ApJ, 804, 96
Gizis, J. E., Burgasser, A. J., Berger, E., et al. 2013, ApJ, 779, 172
Gizis, J. E., Monet, D. G., Reid, I. N., et al. 2000, AJ, 120, 1085
Gizis, J. E., Williams, P. K. G., Burgasser, A. J., et al. 2016, AJ, 152, 123
Guirado, J. C., Azulay, R., Gauza, B., et al. 2018, A&A, 610, A23
Hallinan, G., Antonova, A., Doyle, J. G., et al. 2006, ApJ, 653, 690
Hallinan, G., Antonova, A., Doyle, J. G., et al. 2008, ApJ, 684, 644
Hallinan, G., Bourke, S., Lane, C., et al. 2007, ApJL, 663, L25
Hallinan, G., Littlefair, S. P., Cotter, G., et al. 2015, Natur, 523, 568
Harding, L. K., Hallinan, G., Konopacky, Q. M., et al. 2013, A&A, 554, A113
Horne, R. B., Thorne, R. M., Glauert, S. A., et al. 2008, NatPh, 4, 301
Hunter, J. D. 2007, CSE, 9, 90
Jackman, J. A. G., Wheatley, P. J., Bayliss, D., et al. 2019, MNRAS, 485, L136

Kao, M. M., Hallinan, G., Pineda, J. S., et al. 2016, ApJ, 818, 24
Kao, M. M., Hallinan, G., & Pineda, J. S. 2019, MNRAS, 487, 1994
Kao, M. M., Hallinan, G., Pineda, J. S., Stevenson, D., & Burgasser, A. 2018, ApJS, 237, 25
Konopacky, Q. M., Ghez, A. M., Barman, T. S., et al. 2010, ApJ, 711, 1087
Konopacky, Q. M., Ghez, A. M., Fabrycky, D. C., et al. 2012, ApJ, 750, 79
Lynch, C., Murphy, T., Ravi, V., et al. 2016, MNRAS, 457, 1224
Martin, E. C., Mace, G. N., McLean, I. S., et al. 2017, ApJ, 838, 73
McLean, M., Berger, E., Irwin, J., Forbrich, J., & Reiners, A. 2011, ApJ, 741, 27
McLean, M., Berger, E., & Reiners, A. 2012, ApJ, 746, 23
McMullin, J. P., Waters, B., Schiebel, D., Young, W., & Golap, K. 2007, in ASP Conf. Ser., 376, CASA Architecture and Applications, ed. R. A. Shaw, F. Hill, & D. J. Bell (San Francisco, CA: ASP), 127
Miles-Páez, P. A., Pallé, E., & Zapatero Osorio, M. R. 2017, MNRAS, 472, 2297
Mullan, D. J., & MacDonald, J. 2010, ApJ, 713, 1249
Nichols, J. D., Burleigh, M. R., Casewell, S. L., et al. 2012, ApJ, 760, 59
Osten, R. A., Hawley, S. L., Bastian, T. S., & Reid, I. N. 2006, ApJ, 637, 518
Osten, R. A., Phan-Bao, N., Hawley, S. L., Reid, I. N., & Ojha, R. 2009, ApJ, 700, 1750
Paudel, R. R., Gizis, J. E., Mullan, D. J., et al. 2018, ApJ, 858, 55
Paudel, R. R., Gizis, J. E., Mullan, D. J., et al. 2020, MNRAS, 494, 5751
Perley, R. A., Chandler, C. J., Butler, B. J., & Wrobel, J. M. 2011, ApJL, 739, L1
Phan-Bao, N., Osten, R. A., Lim, J., Martín, E. L., & Ho, P. T. P. 2007, ApJ, 658, 553
Pineda, J. S., Hallinan, G., & Kao, M. M. 2017, ApJ, 846, 75
Pineda, J. S., Hallinan, G., Kirkpatrick, J. D., et al. 2016, ApJ, 826, 73
Potter, D., Martín, E. L., Cushing, M. C., et al. 2002, ApJL, 567, L133
Price-Whelan, A. M., Sipócz, B. M., Günther, H. M., et al. 2018, AJ, 156, 123
Richey-Yowell, T., Kao, M. M., Pineda, J. S., Shkolnik, E. L., & Hallinan, G. 2020, ApJ, 903, 74
Route, M., & Wolszczan, A. 2012, ApJL, 747, L22
Route, M., & Wolszczan, A. 2016a, ApJL, 821, L21
Route, M., & Wolszczan, A. 2016b, ApJ, 830, 85
Sault, R. J., Oosterloo, T., Dulk, G. A., & Leblanc, Y. 1997, A&A, 324, 1190
Schmidt, S. J., Hawley, S. L., West, A. A., et al. 2015, AJ, 149, 158
Schmidt, S. J., West, A. A., Bochanski, J. J., Hawley, S. L., & Kielty, C. 2014, PASP, 126, 642
Schmidt, S. J., West, A. A., Hawley, S. L., & Pineda, J. S. 2010, AJ, 139, 1808
Scholz, R. D. 2014, A&A, 561, A113
Shulyak, D., Reiners, A., Engeln, A., et al. 2017, NatAs, 1, 0184
Siegler, N., Close, L. M., Mamajek, E. E., & Freed, M. 2003, ApJ, 598, 1265
Treumann, R. A. 2006, A&ARv, 13, 229
Turnpenney, S., Nichols, J. D., Wynn, G. A., & Casewell, S. L. 2017, MNRAS, 470, 4274
van der Walt, S., Colbert, S. C., & Varoquaux, G. 2011, CSE, 13, 22
Virtanen, P., Gommers, R., Oliphant, T. E., et al. 2020, NatMe, 17, 261
Williams, P. K. G., & Berger, E. 2015, ApJ, 808, 189
Williams, P. K. G., Berger, E., Irwin, J., Berta-Thompson, Z. K., & Charbonneau, D. 2015a, ApJ, 799, 192
Williams, P. K. G., Casewell, S. L., Stark, C. R., et al. 2015b, ApJ, 815, 64
Williams, P. K. G., Berger, E., & Zauderer, B. A. 2013, ApJL, 767, L30
Williams, P. K. G., Cook, B. A., & Berger, E. 2014, ApJ, 785, 9
Zhang, Q., Hallinan, G., Brisken, W., Bourke, S., & Golden, A. 2020, ApJ, 897, 11